An Airborne Profiling Radar Study of the Impact of Glaciogenic Cloud Seeding on Snowfall from Winter Orographic Clouds

BART GEERTS

Department of Atmospheric Science, University of Wyoming, Laramie, Wyoming

QUN MIAO

Department of Applied Mathematics, Ningbo University, Ningbo, Zhejiang, China

YANG YANG

Department of Atmospheric Science, University of Wyoming, Laramie, Wyoming

ROY RASMUSSEN AND DANIEL BREED

Research Applications Laboratory, National Center for Atmospheric Research, Boulder, Colorado

(Manuscript received 9 March 2010, in final form 25 May 2010)

ABSTRACT

Data from an airborne vertically pointing millimeter-wave Doppler radar are used to study the cloud microphysical effect of glaciogenic seeding of cold-season orographic clouds. Fixed flight tracks were flown downstream of ground-based silver iodide (AgI) generators in the Medicine Bow Mountains of Wyoming. Composite data from seven flights, each with a no-seeding period followed by a seeding period, indicate that radar reflectivity was higher near the ground during the seeding periods. Several physical considerations argue in favor of the hypothesis that the increase in near-surface reflectivity is attributed to AgI seeding. While the increase in near-surface reflectivity and thus snowfall rate are statistically significant, caution is warranted in view of the large natural variability of weather conditions and the small size of the dataset.

1. Introduction

In a 2008 editorial column in *Nature*, it was argued that "... weather modification is one of those areas in which science can have an immediate and obvious benefit for society" (Nature 2008). Cloud seeding probably has been the most widely practiced method of intentional weather modification for the last few decades (e.g., Bruintjes 1999; Qiu and Cressey 2008). It is remarkable that notwithstanding a series of targeted field campaigns and the stronger experimental control than in field work dealing with natural cloud and precipitation processes, the effectiveness of cloud seeding in enhancing precipitation remains uncertain (Ryan and King 1997; Bruintjes 1999; Silverman 2001; National Research Council 2003). Notwithstanding this uncertainty, seeding clouds to enhance precipitation remains a thriving commercial activity, which simply points to the high potential benefit, given the cost of water in water-limited regions. Numerous statistical studies have been conducted to assess changes in surface precipitation, with mixed and questionable results. The level of noise in naturally precipitating cloud systems compared to the magnitude of the signal makes verification of precipitation enhancement extremely difficult (Garstang et al. 2005).

Cloud condensation nuclei are several orders of magnitude more abundant than ice nuclei in the atmosphere, and thus clouds at temperatures well below freezing often consist of water droplets with relatively few ice crystals. On occasion many more ice crystals than ice nuclei are present, most likely because of ice multiplication during riming (Hallett and Mossop 1974). In shallow orographic clouds, ice crystals may also arise from interaction with the underlying terrain (e.g., Rogers and Vali 1987). In a mixed-phase cloud, ice crystals grow at the expense of droplets because of the difference in saturation vapor

Corresponding author address: Bart Geerts, Department of Atmospheric Science, University of Wyoming, Laramie, WY 82071. E-mail: geerts@uwyo.edu

DOI: 10.1175/2010JAS3496.1

pressure at the surfaces of liquid water and ice, which peaks at −12°C. This process, known as the Bergeron (or Wegner–Bergeron–Findeisen) process, is the basis for glaciogenic cloud seeding, whereby ice nuclei such as silver iodide (AgI) particles are injected into a cloud, with the objective of converting the supercooled water into precipitating snow.

While it is easy to demonstrate the efficacy of glaciogenic seeding of nonprecipitating supercooled stratus clouds [e.g., Schaefer (1946), who used dry ice, not AgI], it is difficult to do so in naturally precipitating orographic clouds, which are more complex because of boundary layer turbulence and orographic flows, yet far more important because they produce much of the precipitation in arid, mountainous regions. Altering the ice nucleation process in such clouds also alters other microphysical processes such as riming, leading to poorly understood changes both in cloud composition and in surface precipitation.

Several studies have attempted to document the cloud microphysical ''chain of events,'' starting with Project Whitetop (Braham 1966). A number of experiments have succeeded in documenting AgI plumes and/or microphysical changes within these plumes as they disperse in orographic clouds (e.g., Super and Boe 1988; Super and Heimbach 1988; Deshler et al. 1990; Holroyd et al. 1995; Super 1999; Huggins 2007). These studies generally examined individual cases rather than a population of storms. The results of these studies emphasize the challenges involved in ascertaining the transport and dilution of the AgI nuclei over the target area and in relating changes in liquid water content (LWC) and ice particle size distributions in cloud to seeding activity. Given the complexities of chain-of-events studies, and the statistical uncertainty of outcome-focused randomized experiments (e.g., Morrison et al. 2009), progress is most likely through measurements of cloud microphysical processes by means of instruments not available several decades ago (when most chain-of-events studies were conducted), such as airborne cloud radar.

The objective of this study is to capture changes in radar reflectivity downwind of ground-based AgI generators and to examine whether such changes can be attributed to the AgI seeding. The composite data presented herein will shed some light on the cloud microphysical processes that lead to an alteration of precipitation due to AgI seeding of near-surface orographic clouds. The key tool in this analysis is an airborne high-resolution vertically pointing millimeter-wave Doppler radar. To our knowledge, this is the first time a nadir-pointing airborne radar is used to assess the cloud microphysical impact of glaciogenic seeding. The nadir view provides radar data within ~30 m of the ground, whereas the commonly used ground-based scanning radars can only ''look'' above complex terrain. Ground-based profiling radars, such as the millimeter-wave radar used by Weiss and Hobbs (1974) and Hobbs et al. (1981) to detect seeding effects, have the advantage that they can operate at a lower cost over long time periods, compared to aircraft, but the drawback of frequently missing the seed plume. Our flight patterns were designed to capture a broad range of transport and dispersion patterns (section 2).

This study is relevant not only to the practical question of efficacy of precipitation enhancement by means of glaciogenic cloud seeding, but also to the much broader question about how the concentration of cloud-active aerosol affects the precipitation efficiency of clouds, thereby affecting the latent and the radiative heat forcing of the climate system. The latter question is very complex (e.g., Stevens and Feingold 2009) and thus can be productively addressed by means of relatively controlled experiments such as glaciogenic cloud seeding.

Section 2 describes the experimental design, and section 3 describes the atmospheric conditions during the seven flights. The importance of boundary layer turbulence is addressed in section 4. The relationship between radar reflectivity and snow rate is examined in section 5. Composite reflectivity patterns are presented in section 6. The key finding from this composite comparison (i.e., that AgI seeding enhances near-surface reflectivity) is corroborated with physical arguments in section 7 and with a statistical assessment in section 8.

2. Experimental design

A series of five geographically fixed aircraft tracks (the ''ladder'') was flown repeatedly in winter storms in the vicinity of ground-based AgI generators in the Medicine Bow Mountains of Wyoming, on a total of seven flight days in early 2008 and early 2009 (Fig. 1). These generators were operated as part of the Wyoming Weather Modification Pilot Project (WWMPP), an outcome-focused randomized experiment involving two serially aligned mountain ranges (Breed et al. 2008), one of them the Medicine Bow range. This range is about 30 km across and 1500 m high above the surrounding plains. The aircraft, the Wyoming King Air (WKA), carried in situ cloud microphysics probes, a sensitive 94-GHz (3 mm) Doppler radar with zenith- and nadir-pointing antennas, the Wyoming Cloud Radar (WCR), and a polarization backscatter lidar, the Wyoming Cloud Lidar (WCL).

Three AgI generators were used. None of the seven flights was a case for the WWMPP. Rather, seed operations were controlled as follows: all AgI generators were off for at least 4 h before WKA takeoff. On each of the seven flights, all generators remained off (''no-seed'') for the first 1 or 2 h, and the three select generators were

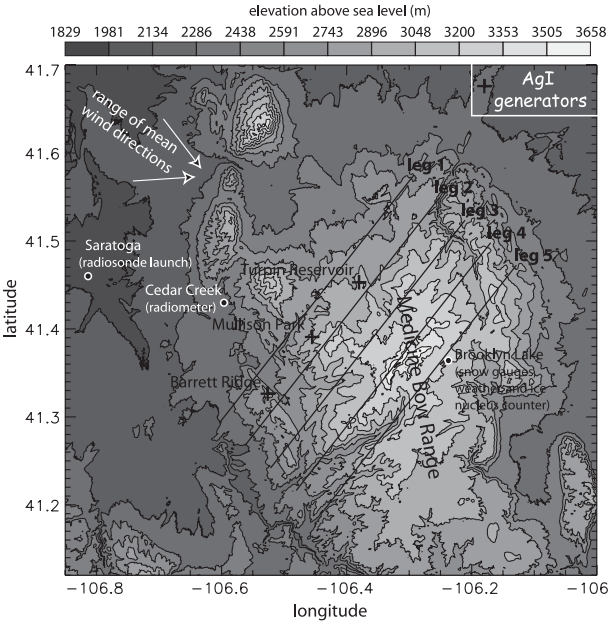

FIG. 1. Terrain map of the Medicine Bow Range in southeastern Wyoming, showing the AgI generator sites, surface measurement sites, and the flight legs. The flight level was 14 000 ft (~4267 m) for all legs.

on (''seed'') for the rest of the flight period (Table 1). The decision to conduct a flight was based on (a) the presence of a persistent winter storm without frontal passage during the duration of the flight, typically 4 h long; (b) an adequately low temperature (at most −8°C at 700 hPa); (c) relatively strong wind (>10 m s^{-1}, on average, between the surface and the mountain top level), to increase the probability that AgI nuclei would be advected rapidly across all four flight legs downwind of the generators; and (d) the direction of the low-level wind. The ideal wind was northwesterly (309°), normal to the five flight legs, a direction that is roughly aligned with the terrain slope. The orientation and length of the legs enabled significant wind direction departures, however (Table 1), which did not preclude encountering the AgI plumes somewhere along the flight leg. The first four flight legs were on the upwind side of the mountain; the last leg generally was on the lee side. The first leg was upstream of the three AgI generators, and the last four were downstream at distances ranging from 2 to 15 km from the generators at each of the legs' closest point. A Vaisala GPS radiosonde was released from Saratoga (mapped in Fig. 1) near the middle of each flight, specifically 1 h 55 min after each WKA takeoff time.

A total of 44 no-seed (70 seed) passes were made along the four downstream legs on the seven flights; the sequence of the leg passes is given in Table 1. The experimental design is intended to minimize differences between the seed and no-seed samples due to terrain or weather variability. A randomized design with some flights taking place entirely during seed operations, and others without any seeding, would have been ill advised in this case given the small number of flights (seven) and the natural variability between storms. In hindsight, the design would have been better if precisely the same number of passes were flown along each leg in each flight in seed and no-seed conditions. This comment will be revisited later (section 7a).

3. Atmospheric conditions during the seven flights

The steadiness and wind direction criteria, used to determine flight times, imply that most cases were postfrontal with little baroclinicity and relatively shallow clouds over the mountain. One exception is 20 February 2009, when a cold front passed during the flight. Low-level clouds generally formed locally over the mountain rather than being advected from afar. Cloud tops were relatively shallow, about 1.5–4.5 km AGL, according to WCR reflectivity profiles summarized in section 6. On all but two days (20 February and 25 March 2009), the Geostationary Operational Environmental Satellite (GOES) infrared cloud-top temperature over the flight ladder varied by less than 11 K, without a clear trend during the flight. On 20 February (25 March) 2009, the cloud-top temperature increased (decreased) by about 18 K during the flight. On some days, cold cloud tops were found rather locally (e.g., 18 February 2009) and on others they were more widespread (Fig. 2). The 10 March 2009 case was particularly cold (Table 1) and cloud-free in the region except for shallow clouds over the mountains.

The bulk Froude number Fr of the upstream flow, calculated based on average upstream conditions between the surface and mountain top level, exceeded unity (Fr > 1) on each of the seven days (Table 1). This implies that the low-level flow was unlikely to be deflected around the mountain (e.g., Smolarikiewicz et al. 1988). Thus, the AgI plumes were likely to be carried over the mountain. We did not have an independent measurement of the transport and dispersion of the seed material over the mountain—for instance, by means of sulfur hexafluoride (SF_6) tracer gas released at the generator sites, a technique used in other experiments (e.g., Bruintjes et al. 1995; Huggins 2007)—but there is some evidence that AgI nuclei were advected over rather than around the mountain.

First, an over-the-mountain flow pattern is confirmed by high-resolution (2 km) model simulations [described by Breed et al. (2008)] for each of the seven days. Secondly, ice nucleus (IN) counter measurements at Brooklyn Lake, a high-elevation site in the lee of the mountain crest (Fig. 1), measured IN concentrations that far exceed the

TABLE 1. Summary of the seven flight days (less-stable days in boldface). The flight legs are numbered and locations are labeled as shown in Fig. 1. The LWC is inferred from a Gerber PVM-100 probe. The LWC and 2D particle probe concentrations are averaged in cloud only (FSSP concentration at least 50 cm^{-3}). The 2D-C concentrations exclude counts in the first bin (~25–50 μm), which is affected by ice crystal shattering. The mean fall speed of hydrometeors is based on a comparison between the air vertical velocity measured by the gust probe and the mean WCR particle vertical motion measured at the nearest radar gate above and below the aircraft, at a range of ~120 m. The snowfall rate is measured by a Vaisala VRG101 gauge in 2008 and a GEONOR T-200B gauge in 2009 at the target site near Brooklyn Lake (Fig. 1). The surface wind is measured at 15 m AGL, above the tree tops. The ice nucleus counter was located 3 km (2 km) southeast of Brooklyn Lake in 2008 (2009). The liquid water path is derived from a two-channel (23 and 31 GHz) radiometer located at Cedar Creek (Fig. 1), with an antenna pointing such that it measures liquid water above the Medicine Bow Range (91° azimuth from north, 10° elevation angle). This slant path is converted to a zenith one (i.e., it represents the vertically integrated liquid water). The sounding data come from a radiosonde released at Saratoga (Fig. 1). The numbers shown in the first five rows under "Saratoga sounding data" represent averages between ground level and the elevation of Medicine Bow Peak. The Brunt–Väisälä frequency N is the dry (moist) value below (above) the cloud base (LCL). Fr is calculated as the wind speed divided by N and the height of Medicine Bow Peak above Saratoga. Ri = N^2/S^2, where S is the magnitude of the shear between the mixed layer (50 hPa deep) and mountain-top level. The elevation of the three generators ranges between 2752 and 2946 m. The mean temperature at the elevation of the generators is estimated from the Saratoga sounding. The direction normal to the five flight legs is 309°.

Flight date	**11 Feb 2008**	**25 Feb 2008**	18 Feb 2009	20 Feb 2009	**10 Mar 2009**	**25 Mar 2009**	30 Mar 2009
Time (UTC)							
WKA starts the first ladder flight pattern	**2003**	**2029**	1644	2154	**1421**	**1613**	1723
WKA ends the last ladder flight pattern	**2256**	**2344**	1959	2410	**1748**	**1927**	2012
Barrett Ridge generator switch-on	**2128**	**2155**	1812	2320	**1454**	**1645**	1754
Mullison Park generator switch-on	**N/A**	**2156**	1815	N/A	**1452**	**1643**	1752
Turpin Reservoir generator switch-on	**2129**	**N/A**	1809	2319	**1456**	**1642**	1750
Flight pattern (see Fig. 1 for leg identification)							
No-seeding leg sequence	**5-4-3-2-1 (2 times)**	**5-4-3-2-1 (2 times)**	5-4-3-2-1 (2 times)	5-4-3-2-1 (2 times)	**5-4-3-2-1**	**5-4-3-2-1**	5-4-3-2-1
Seeding leg sequence	**5-4-3-2-1 (2 times)**	**5-4-3-2-1 (2 times)**	5-4-3-2-1 (2 times)	5-4-3-2-1	**5-4-3 (5 times)**	**5-4-3 (5 times)**	5-4-3 (4 times)
Flight-level data (averages for all passes over legs 2–5)							
Average (maximum) LWC in cloud (g m^{-3})	**0.23 (0.86)**	**0.16 (0.72)**	0.09 (0.33)	0.15 (0.96)	**0.17 (0.53)**	**0.23 (0.79)**	0.13 (0.45)
Average (maximum) 2D-C concentration in cloud (L^{-1})	**8 (50)**	**9 (48)**	10 (28)	21 (49)	**21 (83)**	**17 (43)**	28 (48)
Average (maximum) 2D-P concentration in cloud (L^{-1})	**3 (17)**	**3 (51)**	3 (11)	8 (40)	**1 (16)**	**6 (73)**	7 (33)
Temperature (°C)	**−20**	**−18**	−20	−19	**−28**	**−20**	−25
No-seed flight-level particle fall speed (m s^{-1})	**1.19**	**0.99**	0.80	1.04	**0.91**	**1.02**	0.80
Seed flight-level particle fall speed (m s^{-1})	**1.04**	**0.93**	0.70	0.95	**0.78**	**0.80**	0.72
Brooklyn Lake surface data, Cedar Creek radiometer data, and satellite data (averages during WKA flight period)							
Water-equivalent snowfall rate (mm h^{-1})	**0.60**	**0.31**	1.01	1.17	**0.22**	**0.66**	0.30
Surface wind speed (m s^{-1})	**12**	**14**	10	14	**7**	**9**	10
Surface wind direction (°)	**302**	**278**	283	278	**285**	**276**	313
Ice nucleus concentration (L^{-1})	**N/A**	**45**	11	~100	**~100**	**6**	70
Radiometer liquid water path (mm)	**0.06**	**N/A**	0.08	0.06	**0.03**	**0.12**	0.02
GOES infrared cloud top temperature (°C)	**−28**	**−30**	−32	−36	**−29**	**−37**	−27
Saratoga sounding data (radiosonde released 115 min after WKA take-off)							
Mean wind speed (m s^{-1})	**15**	**12**	14	15	**21**	**14**	11
Mean wind direction (°)	**317**	**293**	300	293	**272**	**265**	323
N (10^{-2} s^{-1})	**0.51**	**0.15**	0.78	0.76	**0.52**	**0.00**	0.61
Fr	**1.9**	**5.0**	1.04	1.2	**2.6**	∞	1.1
Ri	**0.7**	**0.2**	8.1	2.4	**0.4**	**0.0**	3.5
LCL (m MSL)	**2719**	**2782**	2630	2314	**2896**	**2618**	2807
LCL temperature (°C)	**−9**	**−7**	−10	−8	**−19**	**−7**	−16
Temperature at the level of the generators (°C)	**−9**	**−7**	−10	−10	**−17**	**−8**	−15

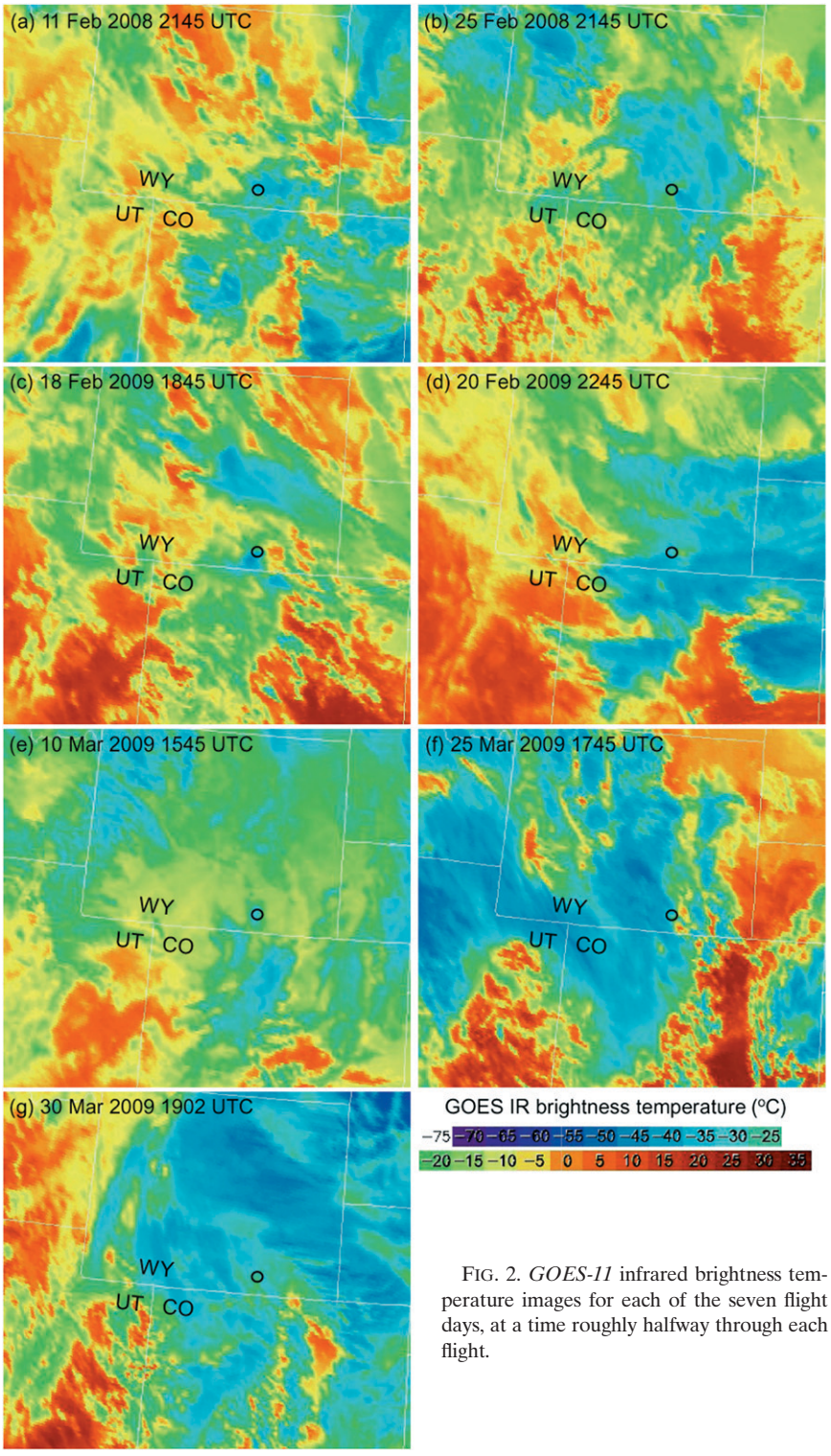

FIG. 2. *GOES-11* infrared brightness temperature images for each of the seven flight days, at a time roughly halfway through each flight.

"background" IN concentration (Table 1), starting shortly after the generators were turned on, on each of the six flight days that the IN counter functioned. An acoustical IN counter of the type described in Super et al. (1988) was in operation as part of the WWMPP. This counter was tuned to detect all IN that activate at temperatures above about −20°C (B. Boe 2009, personal communication). The background was established through IN counter

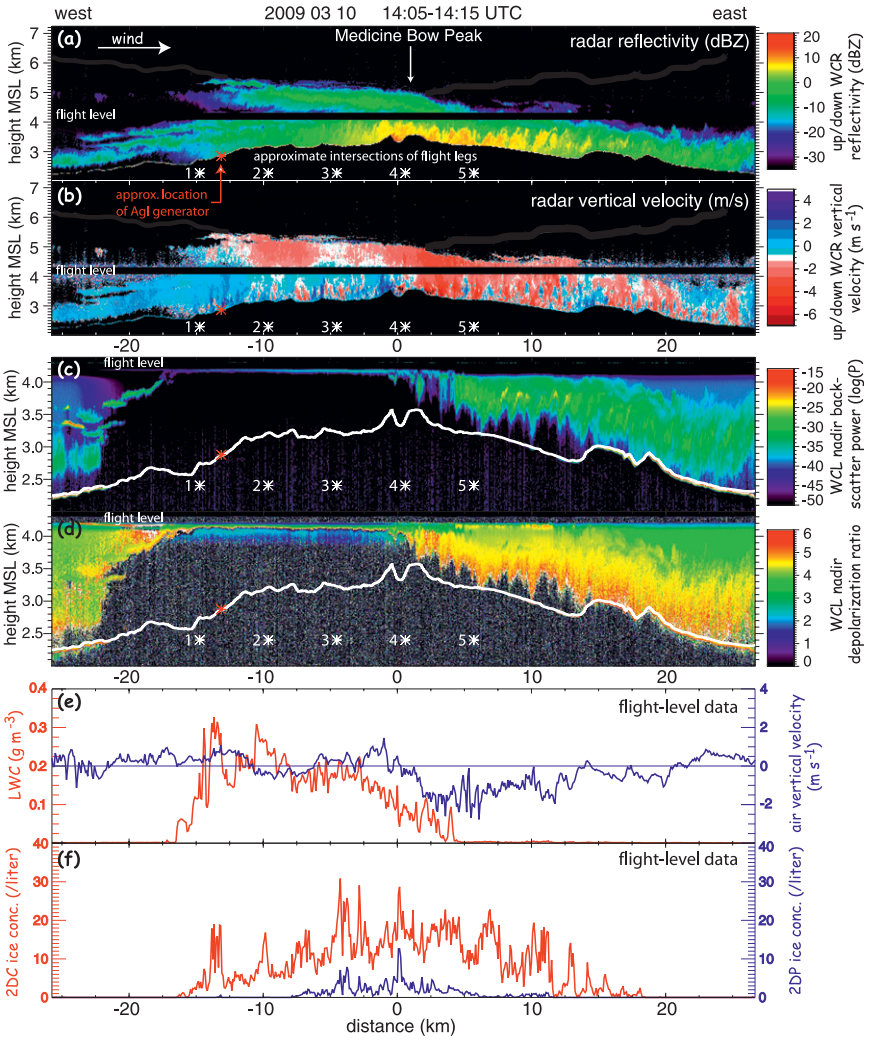

FIG. 3. Example WKA radar, lidar, and in situ data collected along a flight track aligned with the wind over Medicine Bow Peak on 10 Mar 2009. (a),(b) The radar data readily reveal the terrain profile. (c),(d) This profile was added in the nadir lidar transects. (e) The LWC (red) is derived from a Gerber PVM-100 probe; the air vertical velocity (blue) is from the gust probe. (f) The ice concentration is from the 2D-C (red) and 2D-P (blue) probes.

measurements on several clear, unseeded days in the winter of 2008/09. On these days, the IN concentration was less than 1 L^{-1}. Thus, the observed high IN concentrations during the second half of the WKA flights can be attributed to AgI nuclei from any of the generators in use. Note that AgI nuclei can be depleted by nucleation or scavenging, and subsequent precipitation, before reaching the Brooklyn Lake site.

The typically high Froude number was the result of the case selection criteria, which favored strong winds and low stability near the surface. The static stability below mountain-top level was generally low compared to conditions that frequently occur upstream of the Sierra Nevada or Cascades Range during winter orographic precipitation events (e.g., Marwitz 1987; Medina et al. 2005). On four of the seven days (boldface in Table 1) the static stability was particularly low and the vertical shear of the wind strong, such that the bulk Richardson number Ri (calculated between the surface and mountain top level) was close to zero. A low local Ri value implies little resistance to vertical exchange by turbulence.

An example of WCR and WCL profile data is shown in Fig. 3. This flight leg was along the wind, across the five-leg ladder pattern (Fig. 1). Surveillance along-wind legs were flown in the beginning of each flight, and also following the switch-on of AgI generators, to allow time for IN dispersal over the mountain. The flight leg shown in Fig. 3 was flown early in the morning on a cold day with relatively low low-level stability (Table 1). Snow rapidly formed in shallow orographic clouds (Fig. 3c) that

ascended (Fig. 3b) toward flight level on the upwind side, according to the radar (Fig. 3a) and lidar profiles. The rapid attenuation of the lidar backscatter power (Fig. 3c) indicates the top of these clouds. A high depolarization ratio (Fig. 3d) indicates nonspherical particles (i.e., ice crystals). In this transect snowfall was heaviest on the lee side, where the supercooled droplets rapidly evaporated at flight level (Fig. 3e) and below (Fig. 3c), but ice crystals persisted over a long distance. The lack of rapid attenuation and high depolarization ratio values indicate that droplets are absent on the lee side. A further analysis of the lidar data is beyond the scope of this paper. Flight-level particle probe data only record a portion of the orographic cloud and precipitation region.

The base of orographic clouds can be estimated rather accurately from an upstream sounding when well-mixed planetary boundary layer (PBL) flow ascends over the mountain. This cloud base, the lifting condensation level (LCL), compares well (within ± 50 m for each flight) with the cloud-base height estimated by a ceilometer located at Brush Creek (a site just north of the Barrett Ridge AgI generator shown in Fig. 1). It was close to the elevation of the three AgI generators on all seven days (Table 1). The air at this elevation was generally cold enough for a significant fraction of the AgI aerosol to be active ice nuclei (DeMott 1995). The profiles of the WCR equivalent reflectivity factor (referred to as ''reflectivity'' for short) indicate that the orographic clouds produced snowfall at all flight times, even when the AgI generators were off, as was the case for the transect shown in Fig. 3.

The average flight-level LWC in cloud was rather low, ranging from 0.12 to 0.23 g m^{-3} over the seven flights (Table 1). The average Particle Measurement Systems (PMS) 2D-C (2D-P) particle concentration ranged between 8 and 28 (1 and 8) L^{-1}. These averages are based on all passes over the four legs downwind of the generators, irrespective of seeding action. The LWC values are inferred from a Gerber Particle Volume Monitor (PVM-100) probe. The average values from this probe correspond well with those from a Forward Scattering Spectrometer Probe (FSSP) and a Rosemount 871 FA icing probe, within 30%.

Hourly data from WWMPP snow gauges installed at a sheltered location near Brooklyn Lake indicate that snow fell continuously during all flights, with average water-equivalent snowfall rates varying between 0.22 and 1.17 mm h^{-1} (Table 1). There are generally positive correlations among average upwind cloud liquid water path (Table 1), flight-level LWC, the LCL, temperature, and surface snowfall rate, although the two-variable correlations are generally poor and not all positive.

To evaluate weather variability during each flight, WCR reflectivity profiles were used to compute the average near-surface reflectivity and the -20 dBZ echo-top height for all passes over legs 1–5 (Fig. 4). The echo tops were rather low on three days (18 February, 10 March, and 30 March 2009), consistent with the GOES infrared cloud-top estimation (Table 1), except for 18 February 2009, when a thin layer of high cloud was present. This cloud did not seed the orographic cloud below. Generally the near-surface reflectivity was higher over the mountains (legs 4 and 5) than upwind (legs 1 and 2), but there were exceptions. Figure 3 suggests a higher reflectivity across the mountain crest, just in the lee (leg 5), compared to the upwind leg at matching terrain elevation (leg 3), but this is not generally the case: reflectivity generally was higher on leg 3 on 30 March 2009, yet it tended to be higher on leg 5 on 25 March 2009, again with exceptions. Orographic precipitation was rather steady during most flights, except on 25 February 2008, when the storm deepened and intensified, and on 20 February 2009, when the storm top declined. No clear trend in near-surface reflectivity is apparent following the activation of the AgI generators. Some decrease occurred on 10 March 2009, and some increase on 30 March 2009.

4. PBL turbulence

The WCR vertical velocity data indicate that turbulent mixing occurred within the PBL, about 500–1000 m deep in the transect shown in Fig. 3b. The turbulent motion produces vertical velocity variations larger in magnitude than the mountain-scale flow. On the three more stable flight days (Table 1), the PBL top could be readily identified as the top of the turbulent layer, and the WCR vertical velocity pattern suggests a decoupling of the turbulent PBL from the stratified orographic flow pattern aloft. The PBL depth averaged $\sim$650 m on these three days. On the four less stable days turbulent mixing was more intense and deeper, especially on the three flights close to solar noon (11 and 25 February 2008 and 25 March 2009). Sometimes small-scale turbulent updrafts merged to form larger convective updrafts reaching the tops of clouds marked by cumuliform edges.

The PBL turbulence can be expected to effectively mix the AgI nuclei over the depth of the PBL. We derived the 2D flow pattern for all along-wind (across-mountain) flight legs on each of the seven flights, using WCR dual-Doppler syntheses below flight level. This flow pattern (which is the subject of another paper in preparation) suggests that a few air trajectories starting near the surface at the approximate location of the AgI generators (illustrated in Fig. 3a) reached the PBL top before reaching the mountain crest, and that some even made it to flight level. This is consistent with several previous studies that recorded evidence of AgI seeding

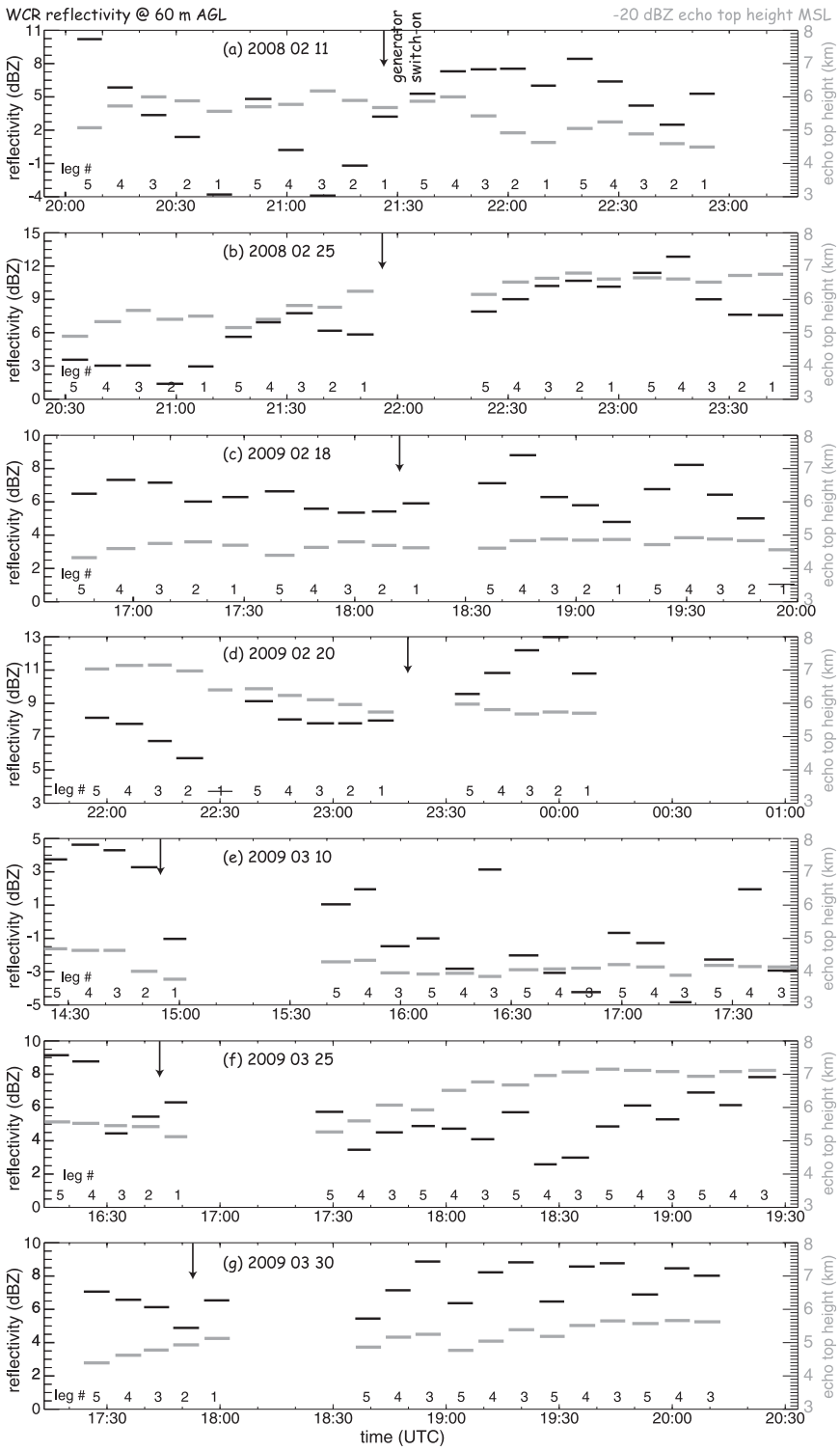

FIG. 4. Average WCR Z at 60 m AGL, and average -20 dBZ echo-top height, for each pass over any of the five legs on the seven flights. The downward arrow indicates the time that the AgI generators were activated.

plumes and/or of a tracer gas released at the AgI generators at flight level (e.g., Holroyd et al. 1988; Super 1999; Huggins 2007). Specifically, in our paper in preparation, we use the probability density function of the WCR dual-Doppler winds (u, w) within the PBL and the estimated hydrometeor terminal fall velocity (Table 1) as the basis for a simple 2D turbulent parcel trajectory model. We find a ~19% probability for nonsedimenting tracers released near the surface at the location of the generators to reach the PBL top at a distance corresponding to leg 5, which is most distant from the generators (Fig. 1), after 20 min on average. The chance for such tracers to make it to flight level at this range was much lower (~4%) because the PBL top usually remained below flight level. Thus, flight-level data over complex terrain are far less useful than remotely sensed data to study the effect of ground-based glaciogenic seeding.

5. W-band reflectivity and snowfall rate

The key strength of the dataset analyzed herein is the radar reflectivity data in very close proximity to the terrain. At 94 GHz (W band) the radar echo is dominated by ice crystals scattering in the Mie regime. This scattering process is complex and highly dependent on crystal shape, orientation, and size distribution (Matrosov 2007). Instead of making assumptions about these parameters and computing the theoretical liquid-equivalent snow rate S corresponding with the observed 94-GHz reflectivity Z, we relate the *observed* WCR Z ($mm^6\ m^{-3}$) near flight level to the *observed* liquid-equivalent S ($mm\ h^{-1}$) at flight level (Fig. 5). The Z value is obtained as an average of the closest radar gates above and below the aircraft. These gates are at a radar range of about 120 m. We compute S from the snow size distributions given by two PMS probes (2D-C and 2D-P), the hydrometeor density, and the observed particle terminal fall velocity (Table 1). The hydrometeor density is estimated from particle size according to the relationship for dry snow particles in Rasmussen et al. (2003) and Rogers (1974).

The snow rates in the orographic clouds generally were quite light at flight level, but a sufficient number of high snow rate values were encountered to reveal a Z–S relationship that reasonably corresponds with the theoretical relationships by Matrosov (2007). These relationships, shown as two purple lines in Fig. 5, give a range of Z–S correspondences, owing to uncertainties in scattering model assumptions. Specifically, Matrosov (2007) obtained this range of Z–S relationships from varying the snowflake's mass, terminal fall velocity, and aspect ratio by ±20% (see his Table 1). The average observed Z–S relationship most closely matches the upper of the two purple lines. The color scheme used in Fig. 5 may

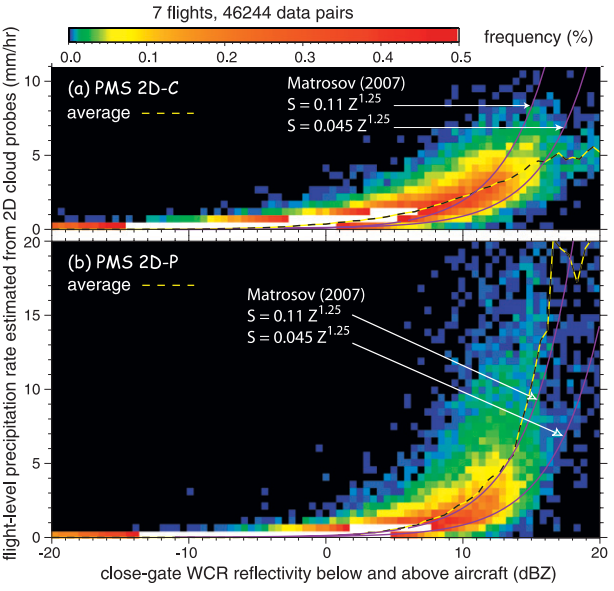

FIG. 5. Scatterplot of flight-level S against near-flight-level Z for all flights. We estimate S from the snow size distributions given by the (a) 2D-C and (b) 2D-P probes, the hydrometeor density, and the particle terminal fall velocity. The abscissa shows the average WCR equivalent Z in the nearest gate above and below the aircraft, at a range of ~120 m. The two purple lines show the range of theoretical Z–S relationships according to Matrosov (2007).

exaggerate the spread of data points. Nevertheless, the variability is substantial, in part because of the spatial mismatch between Z and S measurements and because of the likely variability of 3D shapes and densities of ice crystals. For the purpose of our argument, however, it is sufficient to note that the snow rate tends to increase significantly at WCR reflectivity values over 5–10 dBZ. While such values are rare at flight level, they are far more common near ground level (Fig. 6).

6. Frequency by altitude displays

The 70 seed and 44 no-seed "curtains" of WCR data, at a resolution of ~30 m both in the vertical and along-track dimensions, can be synthesized in the form of a *frequency-by-altitude display* (FAD) (Yuter and Houze 1995). These displays are derived as follows, both for radar reflectivity (Figs. 6a,b) and vertical velocity (Fig. 7). All WCR data collected along the four downwind legs (Fig. 1), excluding the aircraft turns between the legs, are remapped as a function of height AGL, and the occurrences of reflectivity (vertical velocity) values are then counted in bins with dimensions of 0.5 dB ($0.1\ m\ s^{-1}$) and 30 m, for all range gates and all profiles, the total number of which is listed in Figs. 6a and 6b. The vertical resolution (30 m) equals the WCR range resolution. The value shown in Fig. 6a or 6b is this count in each bin, normalized by the total count of all occurrences

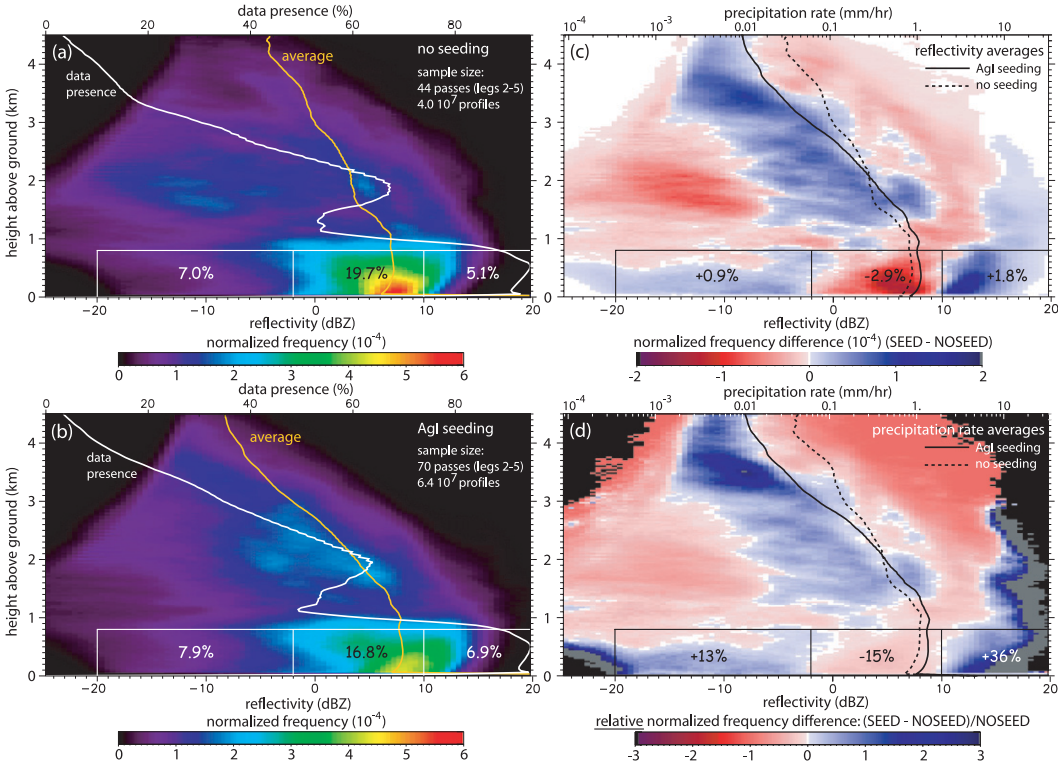

FIG. 6. Normalized FAD of WCR Z for all flight legs downwind of the AgI generators on seven flights, during (a) no-seed and (b) seed conditions. Also shown are cumulative normalized frequencies in three boxes near the ground (%), the mean Z profile, and the "data presence" (i.e., the percentage of WCR range gates with radar echo as a function of height). (c) The difference between the data in (b) and in (a), together with the mean profiles from (a) and (b), and the difference within the three boxes. (d) The ratio of the difference [in (c)] to the no-seed frequency [in (a)], together with the mean profiles of S. We infer S, shown in the upper abscissa of (c) and (d), from $S = 0.11Z^{1.25}$ (Matrosov 2007). In (d), the percentage in each of the three boxes is the ratio of the difference [in (c)] to the no-seed frequency [in (a)] within each box.

in all bins. Thus, the summation of all bin values in Fig. 6a or 6b equals 1.0. The value of such summations in three smaller boxes is also shown in Figs. 3b and 6a. The numbers shown in these boxes actually are percentages of the total: for a box covering the entire domain, the corresponding number would be 100%. The normalized bin values in Fig. 6b are subtracted from those in Fig. 6a to yield Fig. 6c. This difference is divided by the normalized count in Fig. 6a to yield the dimensionless ratio shown for each bin in Fig. 6d. This ratio is also computed within the three boxes and shown as a percentage in Fig. 6d. The "data presence" curves in Figs. 3b and 6a are the percentage of WCR range gates with reflectivity values above the noise level (-25 dBZ) at any height AGL. The depression in the data presence curves between 1.0 and 1.5 km is an artifact due to the radar blind zone centered at flight level. This artifact clearly also affects the FADs, but it does not affect the distribution or mean value at any height. The WCR reflectivity was hardly attenuated by water vapor, by liquid water, or by strong particle scattering because it was quite cold (Table 1), the LWC was low at flight level (Table 1), and the path-integrated reflectivity was relatively weak (Figs. 6a,b), respectively. For instance, the power extinction coefficient at 94 GHz is 4.6 dB km^{-1} per 1 g m^{-3} of cloud water, which includes the extinction by water vapor (Vali and Haimov 1999).

The data presence lines in Figs. 6a and 6b indicate that surface snowfall occurred almost everywhere along legs 2–5 on all passes on all flights irrespective of seeding action. These lines also confirm that the snowstorms were relatively shallow, with the likelihood of measurable reflectivity (thresholded at -25 dBZ) dropping off rapidly above the PBL top to nearly zero at 4.5 km AGL.

At first glance the reflectivity FADs for seed (Fig. 6b) and no-seed (Fig. 6a) conditions are rather similar. Differences are highlighted in three boxes near the surface, shown in each panel of Fig. 6. These boxes have a depth of 800 m, corresponding with the typical depth of the PBL. From right to left, they represent high, medium, and low reflectivity values. Seeding appears to make high as well as low reflectivity values more likely, at the expense of the medium values. The *difference*

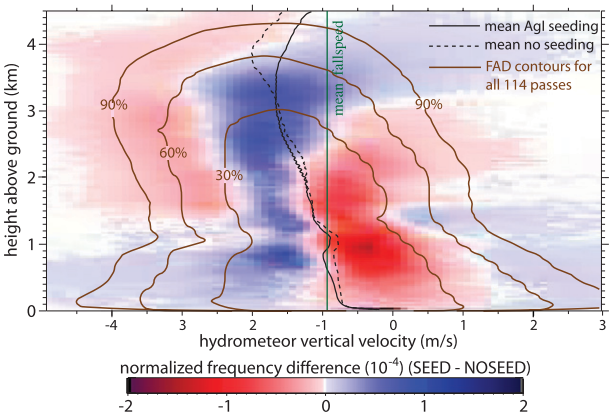

FIG. 7. Seed minus no-seed difference of the normalized FADs of WCR hydrometeor vertical velocity for all flight passes over the legs downwind of the AgI generators on seven flights. The black solid and dashed lines indicate average values for seed and no-seed conditions, respectively. The vertical green line is the observed mean fall speed for seven flights. The brown lines are FAD contours based on all 114 passes (seed and no-seed conditions combined), at three different frequency levels: the outer, middle, and inner contours represent 90%, 60%, and 30% of the cumulative frequency, respectively.

FAD in Fig. 6c highlights this impact. The most prominent feature in Fig. 6c is a dipole near the surface. This dipole suggests that *AgI seeding results in a higher probability of reflectivity values between 10 and 15 dBZ*, and a compensatory reduced probability mainly between 3 and 8 dBZ. The question of cause and attribution will be discussed later.

Differences between seed and no-seed cases also occur aloft, although they are smaller. Above 2 km AGL the mean reflectivity is higher in the no-seed cases than the seed cases (Fig. 6c), implying that the storms tended to be deeper during the no-seed passes. The seed minus no-seed difference can be divided by the normalized no-seed frequency to obtain a relative change (Fig. 6d). This same calculation within the three boxes near the surface indicates that seeding makes high reflectivity values (>10 dBZ) 36% more likely in the PBL. The relative normalized frequency difference for >10 dBZ reflectivity values is even higher closer to the ground.

The average enhancement of reflectivity during seeding is 1.0 dB near the ground (Fig. 6c). This seemingly small difference translates into a significant change in precipitation intensity at the surface. Reflectivity values can be converted to snow rate values using the theoretical relationship in Matrosov (2007) (section 5). We use the upper purple line in Fig. 5, which reasonably fits the observed flight-level Z–S scatter. This exercise indicates that the *average* liquid-equivalent snow rate (whose profile is shown in Fig. 6d) below 800 m AGL is 1.42 mm h^{-1} for the seed cases and 1.13 mm h^{-1} for the no-seed cases, a relative difference of 25%. The same relative difference applies if the lower theoretical Z–S relationship in Fig. 5 is used, since the power (1.25) is the same. Super and Heimbach (1983) found a similar increase in snow rate in AgI seeding plumes over the Bridger Range of Montana in cases where the mountain-top temperatures were below −9°C and the AgI generators were operated in cloud. The precipitation rates mentioned compare well with surface gauge data (Table 1); they are about twice as high, possibly because the target snow gauges were near Brooklyn Lake on the lee side.

Flight leg 1 (Fig. 1) should not be affected by AgI seeding at the three generators under the observed winds. This leg was intended to ascertain any ''pre-existing'' (weather-related) difference between seed and no-seed periods. The average reflectivity along leg 1 is lower than along the four downstream legs (Figs. 6a,b) by a few dBZ especially at low levels, as expected, and there were significant stretches along leg 1 without measurable (>−25 dBZ) echo below flight level. The leg-1 composite reflectivity difference (between seed periods and no-seed periods) can be derived for the first four days only because leg 1 was not flown at all during seeding on the last three days (Table 1). This composite difference (not shown) reveals that storms were generally deeper and stronger in seed periods, which disagrees with the four downstream legs, for which the deeper clouds are observed in no-seed periods (Fig. 6c). The lack of leg-1 passes in the last three days is seen as an important weakness of our experiment. In any event, the leg-1 composite reflectivity difference plot shows consistent enhancement at all levels during seed periods; that is, the average reflectivity profiles during seed and no-seed periods are simply offset from each other by 2–3 dBZ at all levels and do not cross as they do for the downstream legs (Fig. 6c).

The differences shown in Fig. 6 are being interpreted as an AgI seeding impact, but such attribution needs to be thoroughly assessed. We now proceed with such an assessment, first by using physical principles that corroborate this interpretation and next by means of a statistical argument that shows that the observed difference (Fig. 6c) is highly unlikely to be a random result.

7. Support from physical arguments

Cloud particle characterization using in situ probes such as the FSSP, 2D-C, and 2D-P are of limited use since the flight level remains above the PBL in most instances. The flight level varies between 0.6 and 2.1 km AGL with the most common level at 1.2 km AGL, as can be seen in the data presence curve in Figs. 6a and 6b. The prevailing flight level is above the region of reflectivity enhancement (Fig. 6c). Composite differences with in situ

data between seed and no-seed conditions based on all downwind passes on the seven flights are small, as expected, and they are physically plausible in the context of the gust probe vertical velocity differences, which in turn are consistent with WCR vertical velocity differences (Fig. 7) at the corresponding height range. But they bear little if any relation to the ground-based AgI seeding. For instance, there is no evidence for a reduction in supercooled liquid water during the seed periods, according to data from any of the four in situ probes [an FSSP drop size distribution probe, a Rosemount 871FA icing probe, a Gerber PVM-100 probe, and a Droplet Measurement Technology (DMT)-100 hot wire probe]. The 2D-P and 2D-C ice particle concentrations along legs 4 and 5 (where the terrain is highest and the flight level is most likely to intersect the PBL) on the four less stable days (boldface in Table 1) are higher in all size bins during the seed periods, but the difference is unlikely to be statistically significant because of the rather small sample size. Thus, to examine the validity of the AgI seeding effect hypothesis, we focus on WCR data, mainly below flight level.

a. Contrasting population subsets

Ground-based AgI seeding implies that the impact of AgI seeding should be strongest near the ground and within the PBL. This is indeed observed (Fig. 6c). The experimental design—in particular, the presence of both seed and no-seed periods on each flight and the use of geographically fixed flight legs—aims to minimize weather- and terrain-related differences between seed and no-seed periods. Yet some differences can be related to the excess number of seed passes compared to no-seed passes and the uneven distribution of these passes over legs 2, 3, 4, and 5 (Table 1). A reduced sample size with 37 seed and 37 no-seed passes, with matching numbers of passes for each leg, results in a reflectivity difference pattern similar to that in Fig. 6c, with an even higher probability of encountering high reflectivity values during seeding (Fig. 8). The low-level dipole of enhanced probability of $Z > 9$ dBZ and reduced probability of $Z < 9$ dBZ during seeding is even better defined: on average WCR reflectivity is 2.6 dB higher during seeding in the lowest 800 m, as opposed to 1.0 dB for the complete sample (Fig. 6c). According to either of the two Matrosov (2007) Z–S relationships shown in Fig. 5, this reflectivity change implies a doubling of the average low-level snow rate during seeding in the reduced sample, as opposed to a 25% increase for the complete sample. Note that the reduced sample does not capture an increased probability of low reflectivity (<-2 dBZ) near the ground during seeding. There are also some differences aloft between the reduced and complete samples; they can be interpreted in terms of differences in vertical velocity (not shown).

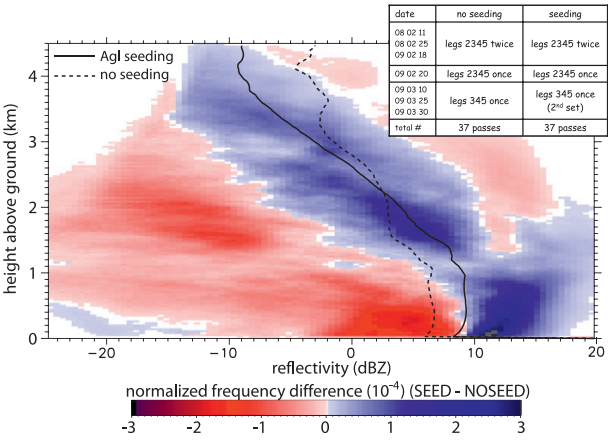

FIG. 8. Difference in normalized FAD of WCR Z between seed and no-seed conditions for a matching number of passes over the four flight legs downwind of the AgI generators. The inset table shows the matching pairs of passes on each of the seven flight days. Also shown are average WCR Z profiles. This figure can be compared with Fig. 6c.

Two partitionings of the entire dataset, based on physical principles, further add credibility to the hypothesis that the low-level snow rate enhancement is the result of AgI seeding. For both, FADs of the type shown in Fig. 6c are examined, with a focus on what we call the *AgI seeding signature*—that is, a higher probability of high reflectivity values and a reduced likelihood of lower reflectivity values near the surface.

On four days the upstream lower troposphere was statically less stable and the bulk Richardson number was very small (Table 1). On these days AgI particles dispersed from the ground were likely to mix over a greater depth of cloud. On the three other, more stable days the PBL was shallower (~650 m) and better defined. The seeding enhancement signature is deep and quite strong on the less stable days, often reaching above flight level and in some cases to a level corresponding with the echo top (Fig. 9). It is concentrated in the PBL on the more stable days. This is consistent with previous studies (Holroyd et al. 1995; Super 1999) that report AgI-seeding-induced ice crystal concentration increases in a shallower layer on more stable days. The storms sampled on these three days were deeper prior to seeding, especially on 20 February 2009. Nevertheless, a clear seeding signature can be seen near the ground. While the seeding signature in less stable conditions is quite distinct from that in more stable conditions well above the ground (mainly between 500 and 1500 m AGL), the average reflectivity enhancement near the surface is about the same (~1.0 dBZ).

The AgI nuclei would reach the flight legs immediately downwind of the generators, legs 2 and 3, after 4–10 min on average, if they moved with the mean wind given in

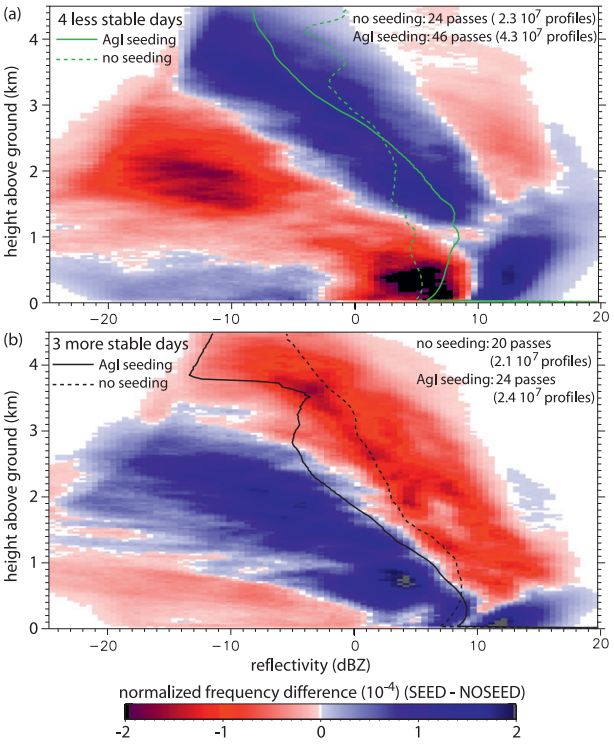

FIG. 9. As in Fig. 8, but for (a) the four less stable days (boldface in Table 1) and (b) the three more stable days.

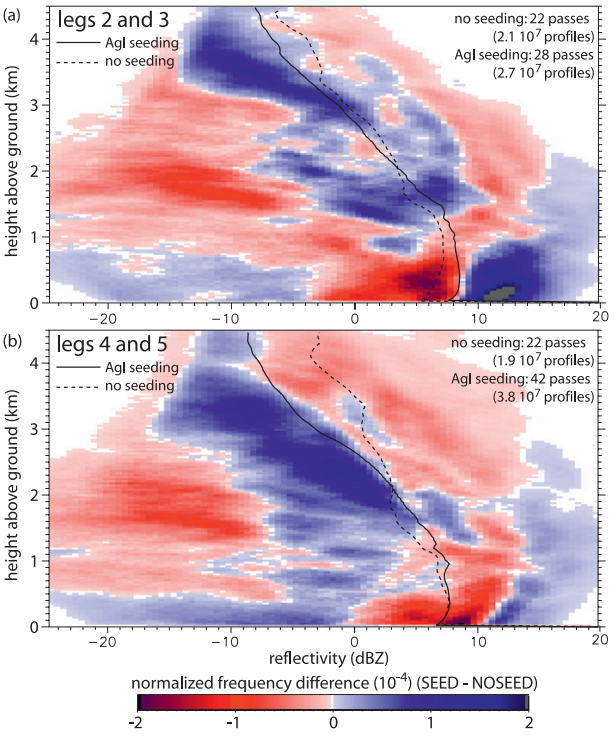

FIG. 10. As in Fig. 8, but for (a) the two downwind legs close to the generators and (b) the two more distant flight legs.

Table 1. The more distant legs 4 and 5 would be reached in 15–21 min on average. These travel times may be underestimated because AgI nuclei are more likely to be found close to the ground than at some 1.5 km AGL, while the mean wind is a linear average for all levels in the sounding between the valley bottom and mountain top level. In any event, virtually all the low-level enhancement of reflectivity observed downwind of the generators occurred along the first two flight legs, rather than along the two more distant legs (Fig. 10). This suggests that ice nucleation and growth on AgI particles occurs rapidly and that these ice crystals grow and fall out relatively close to the generators, consistent with some previous studies. For instance, Holroyd et al. (1995) found that ice crystal concentrations and snowfall rates were an order of magnitude higher just downwind of a ground-based AgI generator compared to more distant sites. They found that the numerous ice crystals in a rather shallow (~1 km deep) orographic cloud close to the generator coalesced into aggregates, which fell out within 20–25 min downwind of the seeding site. Huggins (2007) noted ice particle increases in a seeding plume, as well as a distinct radar echo within the boundaries of this plume, within ~10 km downwind of the AgI generator.

We now examine a third partitioning of the complete sample, which shows, maybe surprisingly, that the enhancement of reflectivity appears to occur not so much within the core AgI plumes directly downwind of the generators, but rather in the peripheral sections (away from the downwind line; Fig. 11). This finding applies both for the two close-proximity flight legs and for the two more distant ones (not shown). Note that the out-of-cone profiles mainly come from the close legs (2 and 3) and are more than twice as numerous as the in-cone profiles (Fig. 11), which mainly come from the distant legs. The composite difference plot shows that within the AgI plumes very light snowfall (<3 dBZ) near the ground was more common during seeding. This could be attributed to an abundance of IN within the AgI plumes, resulting in numerous small ice crystals but no increase in mean reflectivity or snow rate. In other words, local overseeding may have occurred, although there is no direct evidence for this. Two clarifications about the definition of an AgI plume must be made.

First, the actual dispersion patterns of AgI particles are unknown, as mentioned before. Thus, we must resort to a rather arbitrary definition of an AgI plume to make this assessment. Here we define a plume as a 30° cone emerging from a generator in a downwind direction. At any one time the actual AgI dispersion plume probably had a width less than 30°, even on the less stable days. A 30° cone is used nevertheless to account for the

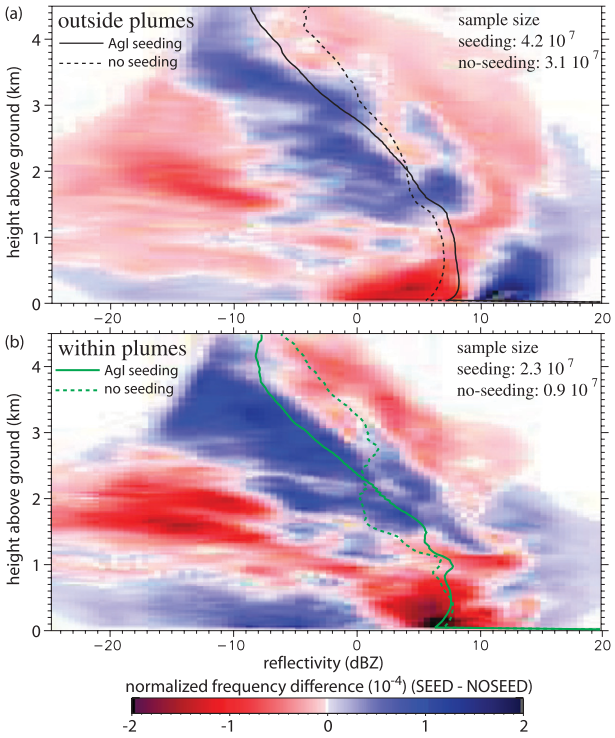

FIG. 11. As in Fig. 8, but for (a) flight leg sections within 30° cones oriented downwind of the generators and (b) flight leg sections outside of these cones. The 30° cones are a surrogate for AgI dispersion plumes during periods of seeding.

uncertainty of the wind measurement and for the high-frequency variability of the turbulent flow. The actual wind direction at any time and/or location may vary substantially from the direction estimated from an upwind radiosonde (Table 1), although a reasonable match with radiosonde wind data is suggested at flight level (where gust probe wind data are available) and also in the turns between the fixed flight legs (where WCR-inferred velocity azimuth display wind profiles are available). We also examined the definition of a plume as a 2-km-wide rectangle whose long axis is in the same direction as the cone. The results for rectangle plumes (not shown) are substantially the same as for cone plumes shown in Fig. 11. A second clarification is that the definition of a plume is the same irrespective of the seeding activity in order to fairly compare seed and no-seed conditions.

b. *Vertical air motion*

Reflectivity differences can also be due to differences in vertical air motions, which are the primary driver of hydrometeor growth and decay. When continental mixed-phase clouds experience strong updrafts ($>\sim$1.0 m s^{-1}), as observed in convection, over local ridges, and in the turbulent PBL, rapid ice particle growth occurs because of the formation of denser particles as a result of riming. The fall speed of the resulting snow tends to be larger than in weak-updraft environments, which favor vapor growth of ice (i.e., the Bergeron process, in which most droplets evaporate before colliding), often followed by aggregation, to yield snow. Within the turbulent PBL strong updrafts are associated with relatively strong downdrafts in close proximity, over spatial scales much smaller than the upwind terrain slope of the Medicine Bow Range ($\sim$15 km), for instance (Fig. 3). This factor and the higher fall speed result in an effective downward transport of hydrometeors. Weak orographic updrafts above the PBL tend to be more widespread and produce lighter precipitation and less dense hydrometeors whose growth time scale may be long compared to the advective time scale over the mountain range.

The WCR vertical velocity data illustrated in Fig. 3 and composited in Fig. 7 are based on raw Doppler velocities corrected for aircraft motion (Leon et al. 2006; Damiani and Haimov 2006). The precise orientation of the antennas relative to zenith and nadir was evaluated by means of the vertical velocity at ground level and, for the up antenna, the continuity of vertical velocity profiles across flight level. The latter led to a +0.6 m s^{-1} adjustment of up-antenna vertical velocities. Vertical velocity data were only included in the composite shown in Fig. 7 where the signal was sufficiently strong (>-25 dBZ).

The WCR does not measure vertical air motion but rather vertical hydrometeor motion. The fall speed of hydrometeors can be estimated by comparing the WCR vertical velocity at close range gates above and below the aircraft to the vertical air motion measured by a gust probe on the aircraft. Average values for seed and no-seed periods are included in Table 1. The composite difference plot shown in Fig. 7 regards the vertical hydrometeor motion. The 7-day mean fall speed (green vertical line in Fig. 7) gives a first-order separation between updrafts and downdrafts: air generally rises (sinks) for bins to the right (left) of this line. Clearly this is a generalization: the actual fall speed probably varies significantly around this average (e.g., Mitchell and Heymsfield 2005).

The brown contours in Fig. 7 are a simplified version of the FAD of WCR vertical velocity, for all passes across legs 2–5 on seven flights. This distribution shows that the vertical velocity variance is larger in the PBL than aloft. Individual WCR cross sections such as the one shown in Fig. 3 show that the width of the vertical drafts is much smaller in the PBL than aloft. Updrafts exceeding 1 m s^{-1} are not uncommon in the PBL (Fig. 7). This suggests that the riming process may be important in the PBL, especially since turbulence boosts collision efficiencies (Khain and Pinsky 1997; Xue et al. 2008). If we continue to ignore variations in fall speed for a moment, then Fig. 7 shows that updrafts were slightly more

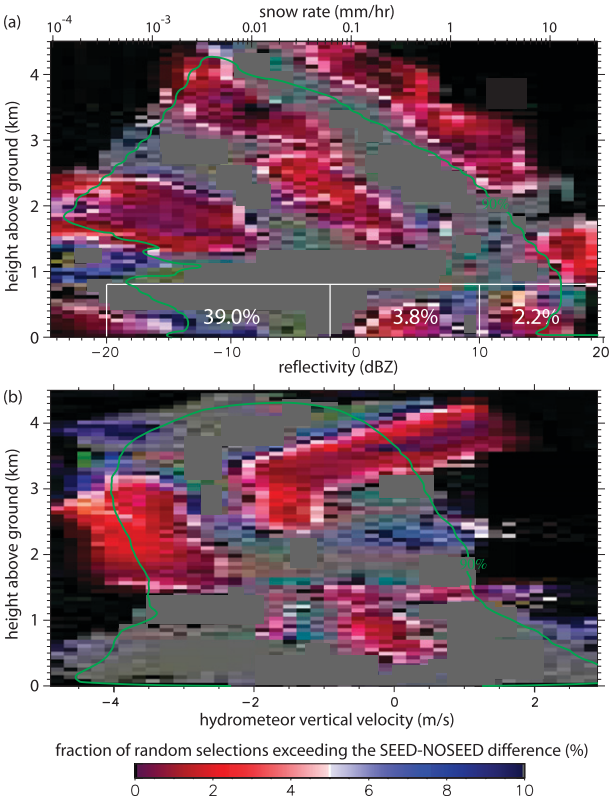

FIG. 12. Percentage of differences between randomly selected subgroups that exceeds the observed seed minus no-seed difference (shown in Figs. 6c and 7) for (a) Z and (b) hydrometeor vertical velocity. The white numbers in (a) are the same values, not at the bin level but within the same boxes as in Fig. 6. In the gray areas, there is a more than 10% probability that the seed minus no-seed difference is by chance. Bins with an absolute normalized seed minus no-seed frequency difference of less than 10^{-5} (usually bins of extremely high or low Z) are shown in black. The green contour comprises 90% of the cumulative data frequency.

common along the no-seed passes at all levels below 3.2 km AGL, with a mean difference of 6 cm s^{-1}.

One might argue that the prevalence of higher vertical motions along the no-seed passes is due to a higher hydrometeor fall speed during seeding. To the contrary, Table 1 indicates that fall speed values were higher in the absence of seeding at flight level, by 12 cm s^{-1} on average. At lower levels, where seeding has more effect, this difference may have been larger. Our interpretation is that the injection of IN in the PBL through AgI seeding suppresses the riming process, enhances the Bergeron process, and thus lowers the hydrometeor fall speed.

Flight-level gust probe data confirm that updrafts were more common along no-seed passes than during seeding. This is consistent with the WCR vertical velocity FAD (Fig. 7), since the flight level is at ~1 km AGL. It is consistent also with the prevalence of slightly deeper storms along no-seed passes (Fig. 6c). One expects an enhanced probability of high reflectivity values near the surface from stronger updrafts and deeper storms. Yet this is not observed (Fig. 6c); instead, high reflectivity values in the PBL were more common during seeding. This counterintuitive anomaly thus is attributed to ground-based AgI seeding.

8. Support from a statistical argument

The probability that random sampling of all flight passes over the four downwind legs yields a normalized reflectivity frequency difference larger than observed in Fig. 6c is shown in Fig. 12a. This probability map is based on random sampling of 70 passes (called group A) and 44 passes (called group B) from the total of 114 passes, irrespective of seeding action. The sampling is done with replacement and is entirely random subject to one condition: that both groups have the same number of passes for each leg as in the seed versus no-seed comparison: that is, group A should have 7, 21, 21, and 21 passes for legs 2, 3, 4, and 5, respectively, and group B should have 11 passes for each leg, as evident from the flight sequences listed in Table 1. This condition is needed in order to eliminate variability due to terrain; for example, a higher reflectivity is expected along leg 4 than leg 2 because it is situated over the crest (Fig. 1), as was the case for the transect shown in Fig. 3. The normalized reflectivity frequency difference (group A − group B) then is computed, as for Fig. 6c. We repeat this experiment 999 times to obtain a probability distribution of normalized frequencies in each bin. The value in any bin in Fig. 6c (Fig. 7) then is compared against this distribution to obtain the probability shown in Fig. 12a (Fig. 12b). For positive (negative) values in any bin in Fig. 6c, the percentage shown in Fig. 12a is the probability that random sampling results in a difference larger (smaller) than the seed minus no-seed value.

This statistical assessment indicates that the observed enhancement of high reflectivity values (>10 dBZ) in the PBL has a 2.2% probability of being by chance; in other words, there is a 97.8% certainty that the increased probability of high snowfall rates during seeding is not by chance. Thus, the near-surface dipole in Fig. 6c is unlikely to be a chance result. There are some other regions where the seed minus no-seed difference is statistically significant (Fig. 12a); some of these occur on the periphery, outside the green contour that encompasses 90% of all data (Fig. 12a). These regions can be ignored because of the unusually high or low reflectivity values. Two other regions occur aloft, within the green contour. These regions clearly result from fortuitous differences in storm depth during the two periods. They overlap somewhat with regions in the corresponding vertical velocity plot (Fig. 12b). We believe that the

regions with statistically significant differences in reflectivity and vertical velocity above the PBL will shrink as the sample size increases beyond the seven flights conducted in the 2008–09 experiment. The important finding is a dipole of statistically significant differences in reflectivity near the ground (Fig. 12a), which is not matched by any statistically significant differences in vertical velocity (Fig. 12b).

9. Conclusions

This study provides experimental evidence from vertically pointing airborne radar data collected on seven flights that ground-based AgI seeding can increase radar reflectivity within the PBL in orographic snow storms. The reflectivity and Doppler vertical velocity data were composited in frequency-by-altitude displays. An increase in low-level reflectivity on the seven flights, each with a no-seed period followed by a seeding period, occurred despite slightly stronger updrafts found on average during no-seeding periods. Theory and a comparison between flight-level snow rate and near-flight-level radar reflectivity both indicate that the observed reflectivity increase just above the surface corresponds with a ~25% increase in snow rate during seeding.

The partitioning of the dataset based on atmospheric stability and proximity to the generators yields physically meaningful patterns and strengthens the evidence. First, the AgI seeding signature is stronger and occurs over a greater depth on the less stable days than on the three more stable days. Second, it is stronger for the two legs close to the generators than for the two distant legs. A random resampling of all flight passes irrespective of seeding action indicates that the observed enhancement of high reflectivity values (>10 dBZ) in the PBL during AgI seeding has a mere 2.2% probability of being entirely by chance.

The results presented have limitations, mainly because just seven storms were sampled and these storms represent a rather narrow region in the spectrum of precipitation systems in terms of stability, wind speed, storm depth, and cloud-base temperature. While the analysis yields strong evidence for an increase in reflectivity near the surface, the quoted change in snowfall rate (25%) is unlikely to be broadly representative. It appears that PBL turbulence over elevated terrain is important for precipitation growth, both in natural and in seeded conditions, and thus the same results may not be obtained if the precipitation growth primarily occurs in the free troposphere. This work needs to be followed up with a longer field campaign under similar as well as more diverse weather conditions. Such campaign should include ground-based instruments, such as vertically pointing or scanning radars and probes to measure ice particle size distribution and density.

Acknowledgments. The seven WKA flights, the radiosondes, and the data analysis were financed by the Wyoming Water Development Commission and the United States Geological Survey, under the auspices of the University of Wyoming Water Research Program. The operation of the AgI generators was supported by the Wyoming Weather Modification Pilot Project (WWMPP), which is coordinated by Barry Lawrence and funded by the State of Wyoming. We thank the WWMPP for operating three AgI generators and launching radiosondes on seven days for our project, at no cost to the authors and at no direct benefit to the WWMPP. Thanks also to those involved with the field work, in particular the Weather Modification Inc. crew, coordinated by Bruce Boe, and the WKA flight crew. The acoustical IN counter data were provided by Bruce Boe. Matthew Pocernich assisted with the statistical analysis. The manuscript benefitted from the comments of Gabor Vali, John Marwitz, Terry Deshler, Jefferson Snider, and Alfred Rodi.

REFERENCES

Braham, R. R., 1966: Final report of Project Whitetop: A convective cloud randomized seeding project. Dept. of Geophysical Sciences, University of Chicago, 156 pp.

Breed, D., M. Pocernich, R. Rasmussen, and R. Bruintjes, 2008: Design of the randomized seeding experiment of the WWMPP. *Extended Abstracts, 17th Joint Conf. on Planned and Inadvertent Weather Modification and WMA Annual Meeting,* Westminster, CO, Amer. Meteor. Soc., 5.3. [Available online at http://ams.confex.com/ams/17WModWMA/techprogram/paper_139159.htm.]

Bruintjes, R. T., 1999: A review of cloud seeding experiments to enhance precipitation and some new prospects. *Bull. Amer. Meteor. Soc.,* **80,** 805–820.

——, T. L. Clark, and W. D. Hall, 1995: The dispersion of tracer plumes in mountainous regions in central Arizona: Comparisons between observations and modeling results. *J. Appl. Meteor.,* **34,** 971–988.

Damiani, R., and S. Haimov, 2006: A high-resolution dual-Doppler technique for fixed multiantenna airborne radar. *IEEE Trans. Geosci. Remote Sens.,* **42,** 3475–3489.

DeMott, P. J., 1995: Quantitative descriptions of ice formation mechanisms of silver iodide-type aerosols. *Atmos. Res.,* **38,** 63–99.

Deshler, T., D. W. Reynolds, and A. W. Huggins, 1990: Physical response of winter orographic clouds over the Sierra Nevada to airborne seeding using dry ice or silver iodide. *J. Appl. Meteor.,* **29,** 288–330.

Garstang, M., R. Bruintjes, R. Serafin, H. Orville, B. Boe, W. Cotton, and J. Warburton, 2005: Weather modification: Finding common ground. *Bull. Amer. Meteor. Soc.,* **86,** 647–655.

Hallett, J., and S. C. Mossop, 1974: Production of secondary ice particles during the riming process. *Nature,* **249,** 26–28.

Hobbs, P. V., J. H. Lyons, J. D. Locatelli, K. R. Biswas, L. F. Radke, R. R. Weiss, and A. L. Rangno, 1981: Radar detection of cloud-seeding effects. *Science,* **213,** 1250–1252.

Holroyd, E. W., J. T. McPartland, and A. B. Super, 1988: Observations of silver iodide plumes over the Grand Mesa of Colorado. *J. Appl. Meteor.,* **27,** 1125–1144.

——, J. A. Heimbach, and A. B. Super, 1995: Observations and model simulation of AgI seeding within a winter storm over Utah's Wasatch Plateau. *J. Wea. Modif.,* **27,** 35–56.

Huggins, A. W., 2007: Another wintertime cloud seeding case study with strong evidence of seeding effects. *J. Wea. Modif.,* **39,** 9–36.

Khain, A. P., and M. B. Pinsky, 1997: Turbulence effects on the collision kernel. II: Increase of the swept volume of colliding drops. *Quart. J. Roy. Meteor. Soc.,* **123,** 1543–1560.

Leon, D., G. Vali, and M. Lothon, 2006: Dual-Doppler analysis in a single plane from an airborne platform. *J. Atmos. Oceanic Technol.,* **23,** 3–22.

Marwitz, J. D., 1987: Deep orographic storms over the Sierra Nevada. Part I: Thermodynamic and kinematic structure. *J. Atmos. Sci.,* **44,** 159–173.

Matrosov, S. Y., 2007: Modeling backscatter properties of snowfall at millimeter wavelengths. *J. Atmos. Sci.,* **64,** 1727–1736.

Medina, S., B. F. Smull, R. A. Houze, and M. Steiner, 2005: Cross-barrier flow during orographic precipitation events: Results from MAP and IMPROVE. *J. Atmos. Sci.,* **62,** 3580–3598.

Mitchell, D. L., and A. J. Heymsfield, 2005: Refinements in the treatment of ice particle terminal velocities, highlighting aggregates. *J. Atmos. Sci.,* **62,** 1637–1644.

Morrison, A. E., S. T. Siems, M. J. Manton, and A. Nazarov, 2009: On the analysis of a cloud seeding dataset over Tasmania. *J. Appl. Meteor. Climatol.,* **48,** 1267–1280.

National Research Council, 2003: *Critical Issues in Weather Modification Research*. National Academy Press, 123 pp.

Nature, 2008: Change in the weather. *Nature,* **453,** 957–958, doi:10.1038/453957b.

Qiu, J., and D. Cressey, 2008: Meteorology: Taming the sky. *Nature,* **453,** 970–974.

Rasmussen, R., M. Dixon, S. Vasiloff, F. Hage, S. Knight, J. Vivekanandan, and M. Xu, 2003: Snow nowcasting using a real-time correlation of radar reflectivity with snow gauge accumulation. *J. Appl. Meteor.,* **42,** 20–36.

Rogers, D. C., 1974: The aggregation of natural ice crystals. Rep. AR 110m, 91 pp. [Available from the Department of Atmospheric Sciences, University of Wyoming, Laramie, WY 82071.]

——, and G. Vali, 1987: Ice crystal production by mountain surfaces. *J. Climate Appl. Meteor.,* **26,** 1152–1168.

Ryan, B. F., and W. D. King, 1997: A critical review of the Australian experience in cloud seeding. *Bull. Amer. Meteor. Soc.,* **78,** 239–254.

Schaefer, V. J., 1946: The production of ice crystals in a cloud of supercooled water droplets. *Science,* **104,** 457–459.

Silverman, B. A., 2001: A critical assessment of glaciogenic seeding of convective clouds for rainfall enhancement. *Bull. Amer. Meteor. Soc.,* **82,** 903–923.

Smolarikiewicz, P. K., R. M. Rasmussen, and T. L. Clark, 1988: On the dynamics of Hawaiian cloud bands: Island forcing. *J. Atmos. Sci.,* **45,** 1872–1905.

Stevens, B., and G. Feingold, 2009: Untangling aerosol effects on clouds and precipitation in a buffered system. *Nature,* **461,** 607–613.

Super, A. B., 1999: Summary of the NOAA/Utah Atmospheric Modification Program: 1990–1998. *J. Wea. Modif.,* **31,** 51–75.

——, and J. A. Heimbach, 1983: Evaluation of the Bridger Range winter cloud seeding experiment using control gages. *J. Climate Appl. Meteor.,* **22,** 1989–2011.

——, and B. A. Boe, 1988: Microphysical effects of wintertime cloud seeding with silver iodide over the Rocky Mountains. Part III: Observations over the Grand Mesa, Colorado. *J. Appl. Meteor.,* **27,** 1166–1182.

——, and J. A. Heimbach, 1988: Microphysical effects of wintertime cloud seeding with silver iodide over the Rocky Mountains. Part II: Observations over the Bridger Range, Montana. *J. Appl. Meteor.,* **27,** 1152–1165.

——, B. A. Boe, E. W. Holroyd, and J. A. Heimbach, 1988: Microphysical effects of wintertime cloud seeding with silver iodide over the Rocky Mountains. Part I: Experimental design and instrumentation. *J. Appl. Meteor.,* **27,** 1145–1151.

Vali, G., and S. Haimov, 1999: Observed extinction by clouds at 95 GHz. *IEEE Trans. Geosci. Remote Sens.,* **39,** 190–193.

Weiss, R. R., and P. V. Hobbs, 1974: The use of a vertically pointing pulsed Doppler radar in cloud physics and weather modification studies. *J. Appl. Meteor.,* **14,** 222–231.

Xue, Y., L. P. Wang, and W. W. Grabowski, 2008: Growth of cloud droplets by turbulent collision–coalescence. *J. Atmos. Sci.,* **65,** 331–356.

Yuter, S., and R. A. Houze, 1995: Three-dimensional kinematic and microphysical evolution of Florida cumulonimbus. Part II: Frequency distributions of vertical velocity, reflectivity, and differential reflectivity. *Mon. Wea. Rev.,* **123,** 1941–1963.